

Enhanced resistance of nanocellular silica to dynamic indentation



Cang Zhao^{a,b}, Yu Qiao^{a,c,*}

^a Department of Structural Engineering, University of California - San Diego, La Jolla, CA 92093-0085, USA

^b X-ray Science Division, Argonne National Laboratory, Argonne, IL 60439, USA

^c Program of Materials Science and Engineering, University of California - San Diego, La Jolla, CA 92093, USA

ARTICLE INFO

Keywords:

Cellular solids
Porosity
Size effect
Impact behavior
Indentation

ABSTRACT

Compared with solids, cellular materials are more lightweight yet usually weaker due to their large porosities. In the current study, it is discovered that the dynamic penetration resistance of nanocellular silica could be effectively higher than that of solid silica when the cell size is smaller than ~100 nm. This phenomenon is attributed to the local hardening that happens when the cell size is sufficiently small and the cell collapse is sufficiently fast. The finding paves a road to the development of strong and lightweight cellular materials.

1. Introduction

Cellular materials are solids containing large volume fractions of empty cells [1,2]. They are widely applied for acoustic insulation, thermal management, catalytic reaction, drug delivery, energy storage, vibration damping, and impact and shock protection [3–7]. A few examples of cellular materials include woods [8,9], bones [10,11], carbon nanotube bundles [12], silica aerogels [13], expanded polymers [14,15], and cellular metals and ceramics [16–19]. They are more lightweight but typically softer and less penetration/indentation resistant than their solid counterparts.

According to the classical theory, the strength, Y , the hardness, H , the stiffness, E , and the toughness, K_c , of a cellular material are related to its porosity, c [1,2,20,21]:

$$(Y, H, E, K_c) \propto (1-c)^\alpha \quad (1)$$

where α is a system constant ranging from 1 to 3; all of them are independent of the cell size, d . In many applications, a low mass density, ρ , is desirable and therefore, the porosity must be maximized [22,23], which however tends to weaken the material. While in some cases using weak cellular materials is acceptable, in general the material must exhibit a sufficiently high strength/hardness; otherwise they cannot meet the increasingly high requirements on structural integrity [24]. In fact, because $\rho \propto (1-c)$ and $H \propto (1-c)^\alpha$, very often the porosity has to be sacrificed to reach the required strength/hardness; these cellular materials are bulky, heavy, and of low performance [25,26].

Over the years, people were searching for solutions of lightweight and hard/strong cellular materials. Particularly, under the most critical

loading conditions, i.e. when the material is impacted, the classical relationship of $H \propto (1-c)^\alpha$ should be broken down. A number of beneficial size effects on the nanometer (nm) scale were investigated for carbon nanotubes [27], nanopillars [28], and nanowires [29]. They have excellent strengths compared with bulk materials, thanks to the low defect density and the beneficial surface phenomena. However, they are small-sized. When they collectively form large cellular structures, e.g. carbon nanotube forests [30], the dominant deformation mechanisms would change and the nm-scale strength may not be proportionally amplified. Nanoporous gold has demonstrated a higher strength than solid gold [31,32], due to the hardening effect associated with the small ligament length; yet, this mechanism is most efficient when the network material is inherently soft and ductile. No conclusive results have been obtained for monolithic cellular materials having intrinsically hard ligaments.

2. Experimental

2.1. Sample processing

Cellular silica samples were fabricated via two sol-gel approaches [33–35]: One for average cell sizes smaller than 500 nm [33]; the other for average cell sizes on the microscopic scale. The cellular morphology was conditioned by a subcritical calcination (SCC) technique [36]. The details of sample processing have been documented elsewhere [36].

For the first sol-gel method, Sigma-Aldrich Ludox HS-40 colloidal silica and PQ Kasil-1 potassium silicate solution, with the total mass of 800 g and the mass ratio in the range from 5:95 to 40:60, were mixed together through magnetic stirring for 30 min. The larger the amount

* Corresponding author at: Department of Structural Engineering, University of California - San Diego, La Jolla, CA 92093-0085, USA.
E-mail address: yqiao@ucsd.edu (Y. Qiao).

of the colloidal silica, the smaller the cell size would be. Next, aqueous solution of formamide (200 g, 40 wt%) was slowly added, and the stirring continued for another 30 min. After that, the solution was poured into a set of polypropylene plastic vials having the inner diameter of 36 mm and the height of 16 mm. After aging for 24 h at room temperature, the wet gels were thoroughly rinsed by a sequential solutions at ~ 90 °C: ammonium nitrate (1 M), nitric acid (1 M), and deionized water. Finally, they were washed by pure methanol at room temperature.

For the second method, Sigma-Aldrich polyethylene glycol (PEG, 32 g) with the average molecular weight of 10,000 was dissolved in aqueous solution of acetic acid (300 ml, 0.01 M). Then, tetramethyl orthosilicate (TMOS, 99%, 150 ml) ordered from Sigma-Aldrich was added under magnetic stirring. After mixing for 30 min, the solution was transported into a set of polypropylene plastic vials having the inner diameter of 46 mm and the height of 22 mm. After aging at 40 °C for 3 days, the wet gels were sequentially rinsed by aqueous ammonia solution (0.1 M) at ~ 120 °C, then by nitric acid (0.1 M) and deionized water at ~ 90 °C, and eventually by pure methanol at room temperature.

In both approaches, every step of the washing process was repeated for at least five times. After that, the solid gels were vacuum dried in an oven (VWR 1330GM) at 80 °C for 3 days. The obtained silica monoliths were fired in a horizontal tube furnace (MTI GSL-1700X) at selected SCC temperatures (1200 °C $\leq T_s \leq 1260$ °C) for 1 h. The initial ramp rate was set to be 3 °C min⁻¹; when the temperature was raised to 100 °C below T_s , the ramp rate was reduced to 1 °C min⁻¹. After SCC, the cooling rate was set as 3 °C min⁻¹. Solid silica disks were employed as reference samples. They were processed through a similar procedure, but were fired at 1250 °C for 12 h.

The SCC-treated silica samples were polished to remove the surface layers by a set of silicon carbide sandpapers [37,38]: 320-grit first, then 600-grit, 1200-grit, and eventually 2500-grit. Before the SCC treatment, the sample thickness was 10–14 mm; after the calcination, the thickness shrank to 7–9 mm. The sample thickness after each step of polishing was 5–6 mm, 5.0 mm, 4.75 mm, and 4.50 mm, respectively. The fabrication conditions of cellular and solid silica samples are summarized in Table 1.

2.2. Sample characterization

The porosity of cellular silica sample was defined as the percentage of volume of empty cells over the total sample volume [1]. It was calculated from the mass density: $c=1-\rho/\rho_n$, where ρ is the sample mass density and $\rho_n=2.2$ g cm⁻³ is the density of solid amorphous silica. Through mercury porosimetry [36], the cell size was estimated from the well-established Washburn equation [36]: $d=4\sigma\cdot\cos\theta/P_{Hg}$, where $\sigma=0.484$ N m⁻¹ is the surface tension of mercury, $\theta\sim 140^\circ$ is the contact angle, and P_{Hg} is the measured mercury infiltration pressure. The measurement results of porosity and cell size are listed in Table 1.

Both cellular and solid silica samples were analyzed by a Bruker D8 Advance Diffractometer with Cu K α radiation ($\lambda=1.5418$ Å). The scan speed was set to be 0.1 s per step; the step size was 0.02°; the 2θ range was 10–80°. Typical x-ray diffraction curves of cellular and solid silica

samples are presented in Fig. 1a. In addition, the cellular silica samples were observed under a scanning electron microscope (SEM, FEI-XL30) at the beam energy of 20 kV and the spot size of 3.0. Prior to the observation, the SEM samples had been coated with iridium at 85 mA for 6 s by an Emitech K575X sputter coater. The cellular structures are shown in Fig. 1(b-d).

2.3. Indentation tests

In this investigation, a home-made indentation testing system was employed to conduct quasi-static and dynamic indentation tests. As shown in Fig. 2a, the indentation system included a front part, a rear part and a hemispherical indenter. The front and rear parts were made of 17-4 PH stainless steel. With their symmetrical configuration, the bending deformation of silica sample during testing could be minimized. An indenter with the diameter of 4.75 mm, the hardness of 91 HRA, and the surface roughness of 0.7 micro inch Ra maximum was used. It was firmly attached to one end of a 17-4 PH stainless steel cylinder by VISHAY M-Bond 200 adhesive. The diameter and the length of the cylinder were 12.7 mm and 25.4 mm, respectively. A silica sample was sandwiched in between the indenter and the steel substrate on the rear part, as illustrated in Fig. 2b. The far end of the steel cylinder would be subjected to either a quasi-static or an impact loading. The lateral surface of the silica sample was confined by two rings: a compliant polyurethane (PU) inner ring, with the initial inner diameter of 19.1 mm and the initial outer diameter of 22.2 mm; and a stiff polyvinyl chloride (PVC) heat-treated outer ring, with the initial inner diameter of 25.4 mm and the shrinking ratio of 2:1.

Quasi-static indentation tests were conducted by compressing the hemispherical indenter into the sample surface using an Instron 5582 machine, as illustrated in Fig. 3a. The loading/unloading rate was 0.01 mm min⁻¹, and the peak loading force was 300 N. Typical force-displacement curves are shown in Fig. 3b. For each type of silica, at least three samples were tested.

An impact system, as illustrated in Fig. 4a, was employed to provide dynamic indentation and compression loadings [7,39–41]. The details of the impact system and the results of dynamic compression tests have been documented in Supplementary material. A titanium (Ti) tube striker with the total mass of 63 g was projected from a high-pressure gas chamber to impact a stainless steel (17-4 PH H900) incident bar. The striker speed was measured to be ~ 8.5 m s⁻¹ for all the tests by a set of photomicro sensors (OMRON EE-SPW421). The incident bar then compressed a hemispherical indenter into the silica disk sample. The silica sample was firmly supported by a stainless steel substrate, followed by the transmitted bar. The diameter of the indenter was 4.75 mm. The diameters of the incident and the transmitted bars were the same 12.7 mm. Two sets of strain gauges (Vishay WK-13-250BF-10C) were mounted at the center of the two bars respectively to record stress wave profiles through a data acquisition system (Vishay 2310B). Typical incident and transmitted stress wave profiles are shown in Figs. 4b and 4c, respectively. The loading mode was similar with that of the quasi-static indentation experiment, while the loading rate was much higher. For each type of silica, at least three samples were tested.

Table 1

Synthesis parameters and properties of cellular and solid silica samples.

Mass ratio of reagents	TMOS to PEG	Colloidal silica to potassium silicate							
		5:95	10:90	15:85	18.5:81.5	25:75	30:70	40:60	25:75
SCC temperature [°C]	1210	1249	1254	1247	1236	1236	1229	1224	1250 (12 h)
Sample thickness [mm]	4.52 \pm 0.01	4.54 \pm 0.01	4.53 \pm 0.01	4.54 \pm 0.01	4.53 \pm 0.01	4.54 \pm 0.01	4.53 \pm 0.01	4.54 \pm 0.01	4.54 \pm 0.01
Cell size range [nm]	[390,1010]	[210,340]	[170,250]	[135,200]	[120,170]	[90,120]	[70,90]	[40,60]	Solid silica
Average cell size [nm]	700 \pm 440	275 \pm 90	210 \pm 60	165 \pm 45	145 \pm 35	105 \pm 15	80 \pm 15	50 \pm 10	Solid silica
Porosity [%]	59.7 \pm 1.0	60.7 \pm 1.2	59.9 \pm 0.6	59.8 \pm 1.2	60.6 \pm 1.1	61.4 \pm 1.4	60.5 \pm 0.5	60.5 \pm 0.5	< 1.0

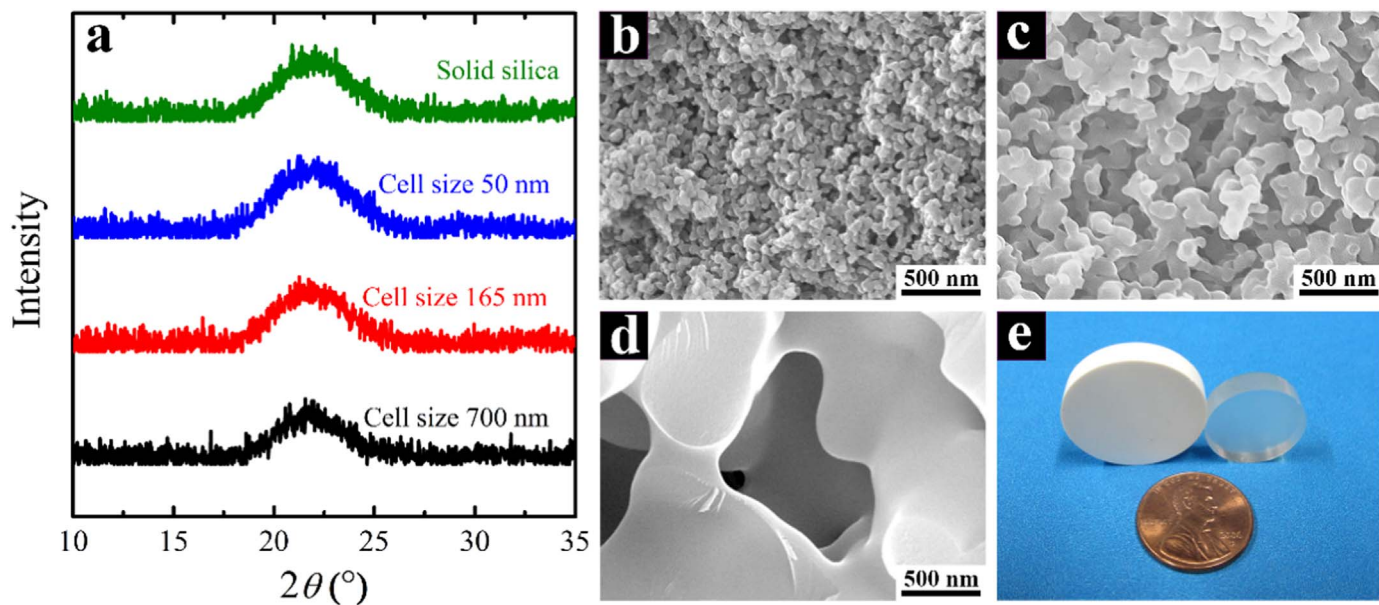


Fig. 1. Cellular and solid silica samples. (a) Typical powder x-ray diffraction curves. SEM images of cellular silica having the average cell sizes of (b) 50 nm, (c) 165 nm, and (d) 700 nm, respectively. (e) Photographs of a cellular (left) and a solid (right) silica sample.



Fig. 2. Indentation testing system. (a) The system components and a cellular silica sample. The diameter of the sample is ~23 mm. (b) A cellular silica sample mounted in the indentation testing system. Part of the mounting parts are removed and the front part is lifted up to show the contact between the indenter and the sample surface.

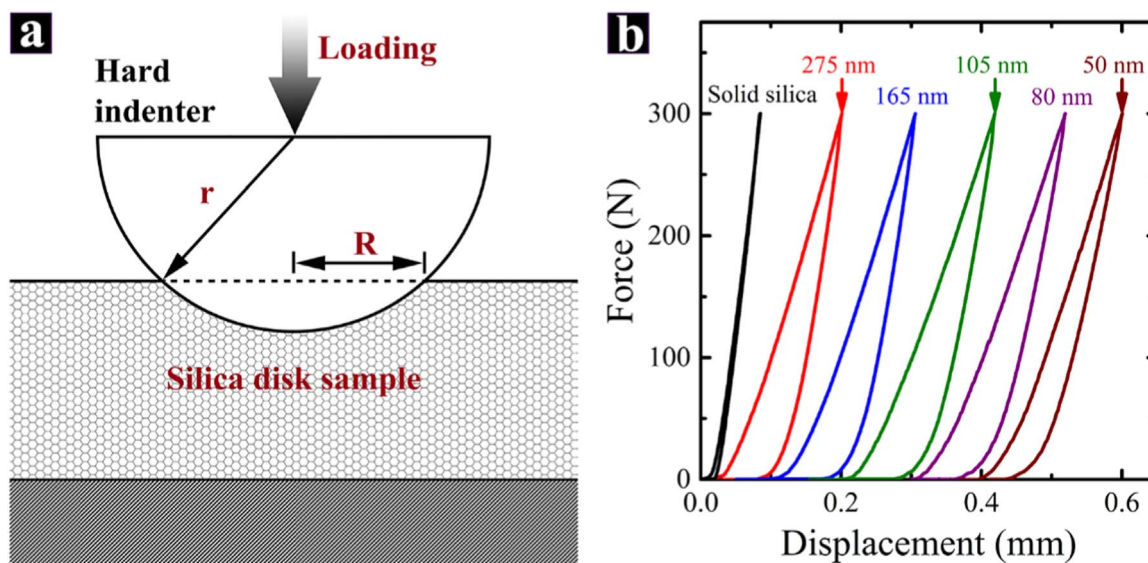


Fig. 3. Quasi-static indentation tests. (a) Schematic of the quasi-static indentation setup. (b) Typical indentation curves. The curves have been shifted along the horizontal axis. The arrows indicate the average cell sizes.

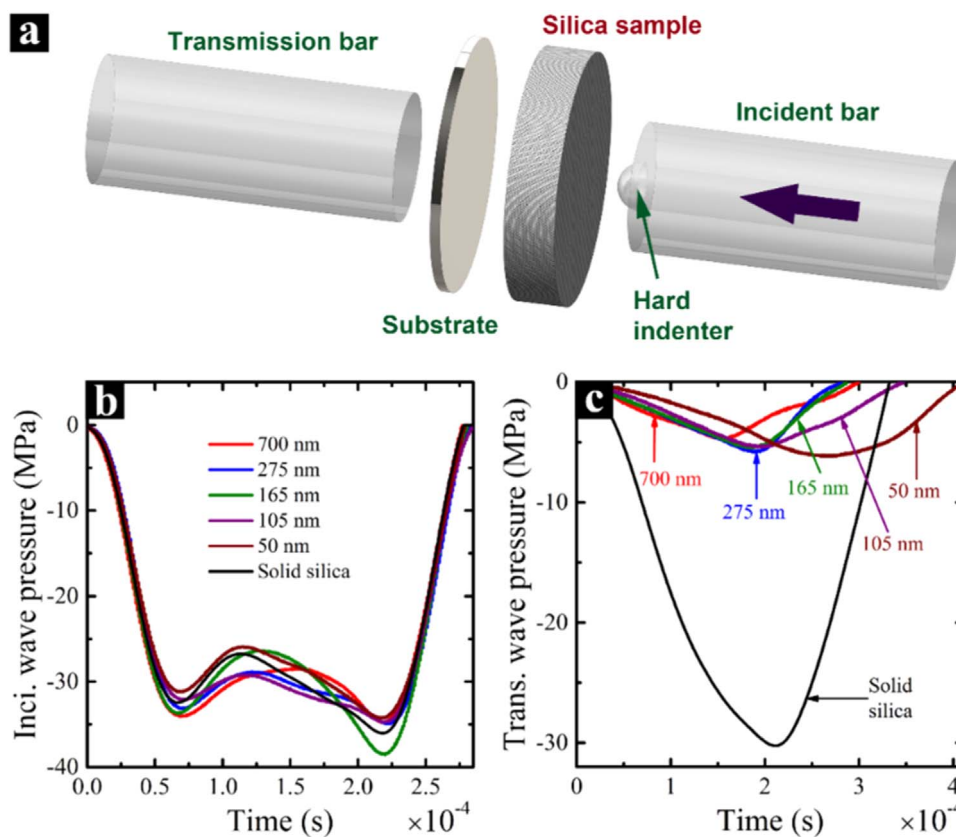


Fig. 4. Dynamic indentation tests. (a) Schematic of the dynamic indentation setup. The arrow in the striker indicates the impact direction. Typical profiles of (b) incident and (c) transmitted stress waves. The arrows indicate the average cell sizes. (For interpretation of the references to color in this figure legend, the reader is referred to the web version of this article.)

2.4. Indentation characterization

After the indentation tests, the sample surfaces were observed by a Keyence VHX-1000 Digital Microscope. Through its built-in function of “3D Image Stitching”, the depth profiles of quasi-static and dynamic indentations were scanned, as shown in Fig. 5b and Fig. 6b, respectively, with the scanning range slightly broader than the difference between the highest and the lowest focusing points. The scanning resolution was less than 2 μm per step. The indentation sizes (R) were then measured from the sample surfaces (Figs. 5a and 6a), and the

results are presented in Figs. 5c and 6c.

Additionally, after dynamic indentation, as shown in Fig. 8a, the lateral inner surfaces of selected silica samples were exposed by cleaving along their diameters, and the areas of interest were observed under a FEI-XL30 SEM (Fig. 8(b-d)). The SEM samples, prior to the observation, had been coated with iridium by an Emitech K575X sputter coater (85 mA, 6 s). Typical cellular structures in the cell deformation zones (CDZ), the transition zones (TZ), and the far fields of dynamically indented cellular silica samples are summarized in the insets (P1-P3) to Fig. 8c and Table S1-S3 in Supplementary material.

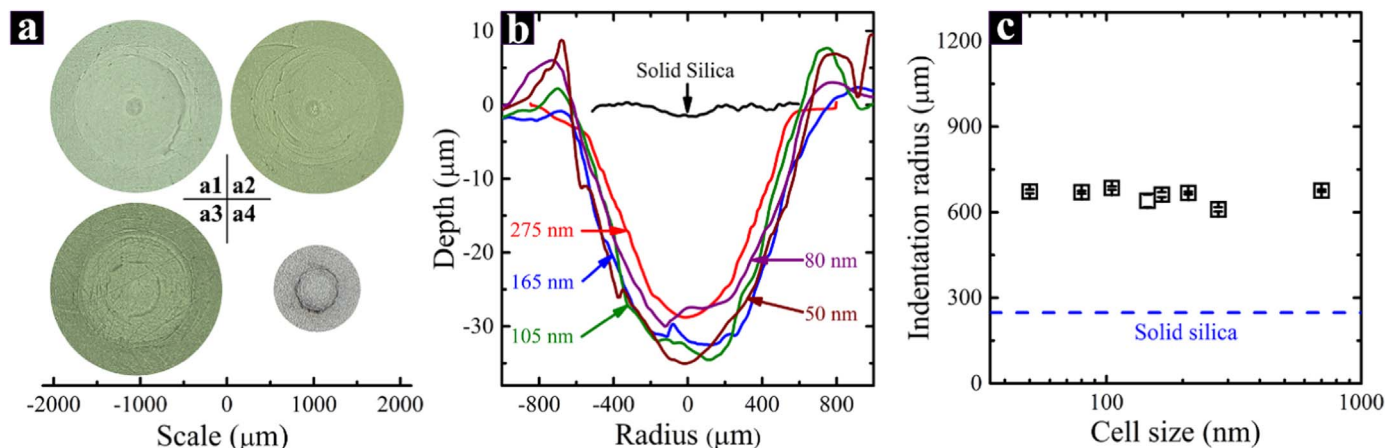


Fig. 5. Profiles of quasi-static indentation. (a) Photos of quasi-statically indented cellular silica samples with the average cell sizes of (a1) 275 nm, (a2) 105 nm, and (a3) 50 nm, respectively; (a4) is a solid silica sample. (b) Typical indentation depth profiles of quasi-statically tested samples. The arrows indicate the average cell sizes. (c) Indentation radius as a function of the average cell size. The dashed line shows the average indentation radius of solid silica samples, with the standard deviation less than 2 μm . (For interpretation of the references to color in this figure legend, the reader is referred to the web version of this article.)

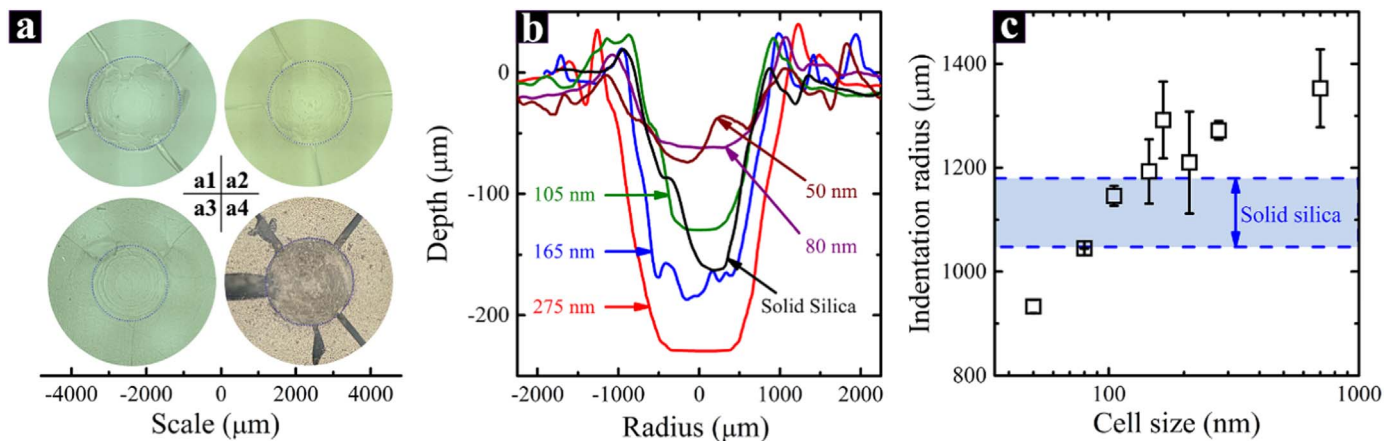


Fig. 6. Profiles of dynamic indentation. (a) Photos of dynamically indented cellular silica samples with the average cell sizes of (a1) 275 nm, (a2) 105 nm, and (a3) 50 nm, respectively; (a4) is a solid silica sample. (b) Typical indentation depth profiles of dynamically tested samples. The arrows indicate the average cell sizes. (c) Indentation radius as a function of the average cell size. The horizontal band within the two dashed lines shows the range of indentation radius of solid silica.

Table S4 in Supplementary material shows the typical morphology of dynamically indented solid silica.

3. Results and discussion

As shown in Table 1, the testing samples are in the disk form, having the thickness of ~ 4.50 mm and the diameter of ~ 23 mm. By taking advantage of the difference between the temperature sensitivities of the cell size, d , and the porosity, c , these two parameters have been separately adjusted [36]. As the SCC temperatures are optimized, the porosities of all the cellular silica are controlled to be around 60%, while their average cell sizes range from ~ 50 nm to ~ 700 nm and the pore size distributions are relatively narrow [42]. As reference samples, the porosities of solid silica are measured to be less than 1%. The X-ray diffraction analysis, as presented in Fig. 1a, confirms that the ligaments of all the cellular samples are in the same amorphous phase as the solid silica. In Fig. 1(b–d), the cells are interconnected and of similar configurations; the ligament length is nearly proportional to the cell size.

In Fig. 5c, it can be seen that, under the quasi-static indentation loading, the responses of all the cellular silica samples are similar. No clear correlation can be identified between the indentation size, R , and the cell size, d . The indentation created in solid silica under the same loading conditions is much smaller, which should be attributed to its much higher quasi-static resistance to penetration, i.e. hardness. For all the cellular silica samples, regardless of the cell size, the indentation size, R , is around $660 \mu\text{m}$. The indentation size of solid silica is nearly $250 \mu\text{m}$.

Quasi-static hardness of a material, H , can be assessed through [26,43,44]

$$H = F_{\max}/\pi R^2 \quad (2)$$

For a cellular material, under the same loading conditions, combining Eq. (1) and Eq. (2), we have

$$1/\bar{R}^2 \propto (1-c)^\alpha \quad (3)$$

which can be rewritten as

$$\bar{R} \propto (1-c)^{-\alpha/2} \quad (4)$$

where $\bar{R}=R/R_s$ is the normalized indentation size, with R_s being the indentation radius of solid silica. Apparently, the normalized indentation radius increases with the porosity. In this investigation, all the cellular silica samples have a similar porosity of $\sim 60\%$; in Fig. 5c, the indentation size of solid silica is $\sim 40\%$ of that of cellular silica. Therefore, the system constant, α , could be determined to be ~ 2 , according to Eq. (4).

For self-comparison purpose, we define a nominal indentation resistance (NIR) index:

$$\theta = 1/\bar{R}^2 \quad (5)$$

The smaller the normalized indentation radius, the larger the NIR index, and the higher the resistance to indentation/penetration. In the following discussion, the NIR index under quasi-static loading is denoted as θ_q ; under dynamic loading, it is denoted as θ_d . In Fig. 7a, for the cellular silica samples under investigation, the indexes, θ_q , are always around 0.14, regardless of the variation in cell size, d , agreeing well with the classical theory for open cellular materials (Eq. (3)) [1,2].

However, under dynamic loading, the behavior of nanocellular silica significantly changes, and cell size becomes an important factor. As presented in Fig. 6c, when the cell size is above 165 nm, the dynamic indentation size of cellular silica is larger than that of solid silica; that is, with the large porosity $\sim 60\%$, a cellular silica tends to be softer than its solid counterpart. However, when the cell size is reduced to below 165 nm, the indentation size rapidly decreases with d , which suggests that nanocellular silica with a smaller cell size tends to be effectively “harder”. Eventually, when d is smaller than ~ 100 nm, the dynamic indentation size of nanocellular silica is smaller than that of solid silica.

The dynamic NIR indexes (θ_d) of cellular silica samples are shown in Fig. 7b. As the cell size decreases from 700 nm to 165 nm, θ_d increases while the change is within the data scatter. As the cell size varies from 165 nm to 50 nm, θ_d largely rises from 0.9 to 1.4 by more than 50%. Particularly, as the cell size is below ~ 100 nm, θ_d is above 1, suggesting a higher resistance to dynamic indentation/penetration compared with solid silica.

Since the experimental data suggests that θ_d is dependent on the cell size (d) and the loading rate (v), and is also related to the quasi-static hardness (H), we have

$$\theta_d = f(d, K, H) \quad (6)$$

where K is the impact energy and f is a certain function. According to the Π -theorem [45],

$$\theta_d/\theta_q = f(K/Hd^3) \quad (7)$$

If f is taken as a power law,

$$\theta_d/\theta_q \propto (K/Hd^3)^\beta \quad (8)$$

where it is assumed that

$$K \propto v^2 \quad (9)$$

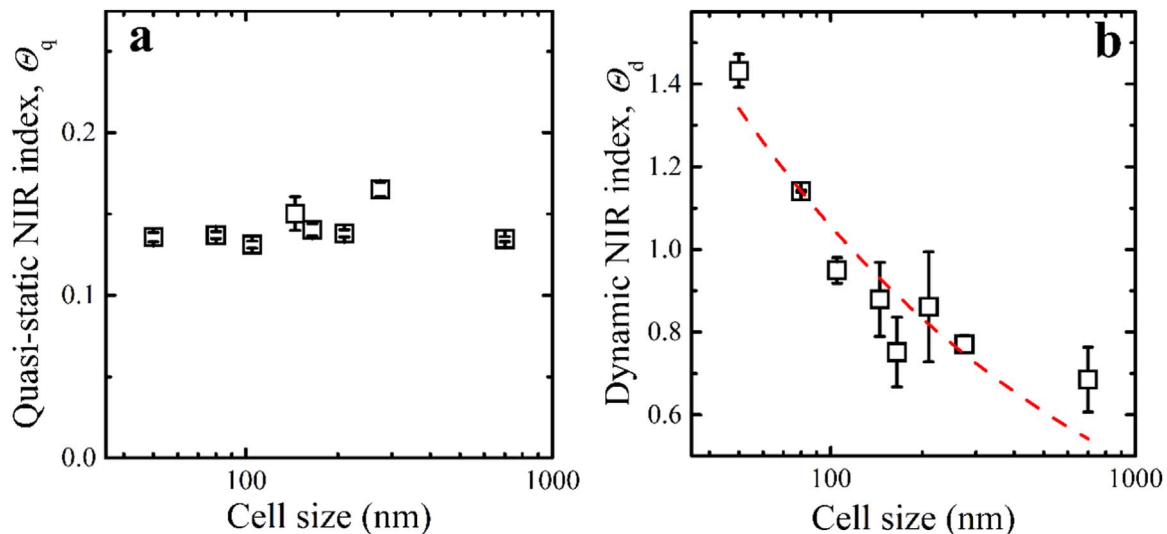


Fig. 7. Nominal indentation resistance (NIR) index as a function of the average cell size under (a) quasi-static and (b) dynamic loadings. The quasi-static loading rate is 0.01 mm min^{-1} , and the dynamic striker speed is $\sim 8.5 \text{ m s}^{-1}$. The open squares show the experimental data, with the error bars being the standard derivations. The dashed line in (b) is the regressed curve, with the power law form of $d^{-3\beta}$ ($\beta=0.10$).

with v being the impact velocity. Combination of Eqs. (1), (3), (5), (8) leads to

$$\Theta_d \propto \left(\frac{v^2}{d^3}\right)^\beta (1-c)^{\alpha(1-\beta)} \quad (10)$$

where $\beta \geq 0$ is a system parameter. When $\beta=0$, Eq. (10) is reduced to Eq. (3), and the NIR index is not dependent on the cell size, d ; when β is positive, not only the influence of the porosity, c , is weaker by a power of $\alpha\beta$, but also a new factor, v^2/d^3 , comes in. While the increase in c tends to decrease Θ_d , if v is sufficiently high and d is sufficiently small, Θ_d could be larger than 1; i.e. under dynamic loading, the effective resistance to indentation/penetration of a nanocellular material could be effectively higher than that of a solid. In Fig. 7b, through data fitting, the value of β is determined to be 0.10 ± 0.01 .

This “counter-intuitive” cell size effect indicates that upon impact and when the cell size is below $\sim 100 \mu\text{m}$, the classical theory (Eqs. (1) and (3)) breaks down. The underlying mechanism is revealed on the level of microstructures, as shown in Fig. 8 and Table S1–S3 in Supplementary material. Underneath the indentation, the material is compacted and the cellular structures are highly deformed; the local area in which more than 50% of cells are crushed (e.g. P1 in the inset to Fig. 8c and Table S1) is defined as the cell deformation zone (CDZ) and their boundaries are marked out by the solid squares and the red solid line; in the far field, the cells are pristine (e.g. P3 in the inset to Fig. 8c and Table S3), and the boundaries are shown by the hollow squares and the green dashed line; in between the far field and the CDZ, there is a transition zone (TZ) where the deformation of the cellular structures is permanent yet relatively mild (e.g. P2 in the inset to Fig. 8c and Table S2). For all the cell sizes under investigation, the depth of CDZ is quite similar, around $1500 \mu\text{m}$. The CDZ width decreases with the reduction in cell size, following the trend of indentation radius. A major difference between the large cell size above 165 nm and the small cell size below 100 nm is associated with the TZ: When the cell size is relatively large, the volume of the TZ is negligible; when the cell size is relatively small, the TZ becomes much broader. When the cell sizes are $\sim 100 \text{ nm}$ and $\sim 50 \text{ nm}$, the depths and the widths of the TZ are $350\text{--}450 \mu\text{m}$ and $200\text{--}350 \mu\text{m}$, respectively. The existence of TZ implies that, as the indenter impacts the sample, the resistance to the motion of the indenter comes from not only the CDZ, but also the TZ. For small cells, when the indenter moves into the silica sample surface, it has to overcome the additional resistance offered by the large volume of material in the TZ and consequently, the indentation depth and size

becomes smaller. The measurement results of dynamic NIR index (Fig. 7b) and the SEM image analysis (Fig. 8) agree with each other. Compared with cellular silica, the dynamically indented solid silica, as presented in Table S4 in Supplementary material, exhibits typical hackle markings [46,47]. Note that the structure of TZ is somewhat similar with the “cold” boundary layer observed in granular materials [48,49]; however, the mechanisms of dynamic deformations of cellular and granular materials are distinct.

The nanocellular silica behavior under the dynamic indentation loading is highly nonlinear since the cells in the CDZ are crushed and the material properties are permanently changed, and highly localized since the impact front is non-uniform [50,51]. Upon impact, the compaction of smaller cells is completed faster than larger ones. Firstly, when the cell size is relatively small (e.g. much smaller than the characteristic length scale of the indentation front), the cell collapse would result in local densification, instead of local deflection. Secondly, this locally hardened layer would suppress the shear instability [7] and transfer the impact energy into the surrounding material [52], resulting in the development of TZ. The TZ not only enhances the resistance to dynamic indentation, but also increases the energy absorption capacity, as reflected in Fig. 4c that the amplitude of transmitted wave increases with the reduction in cell size.

4. Conclusions

In summary, under the dynamic indentation condition under investigation, it is discovered that when the cell size of a nanocellular silica is below $\sim 100 \text{ nm}$, regardless of the large porosity of $\sim 60\%$, the resistance to indentation could be effectively higher than that of solid silica. A theoretical analysis suggests that as the impact rate is sufficiently high and the cell size is sufficiently small, the penetration/indentation resistance is no longer governed only by the classical law of porosity; rather, the impact rate and the cell size play critical roles. This unique phenomenon is attributed to the local hardening ahead of the impact indenter associated with the fast collapse of nanocells. The finding sheds light on the development of strong and lightweight cellular materials.

Acknowledgements

This research was supported by The Army Research Office under Grant No. W911NF-12-1-0011, for which the authors are grateful to

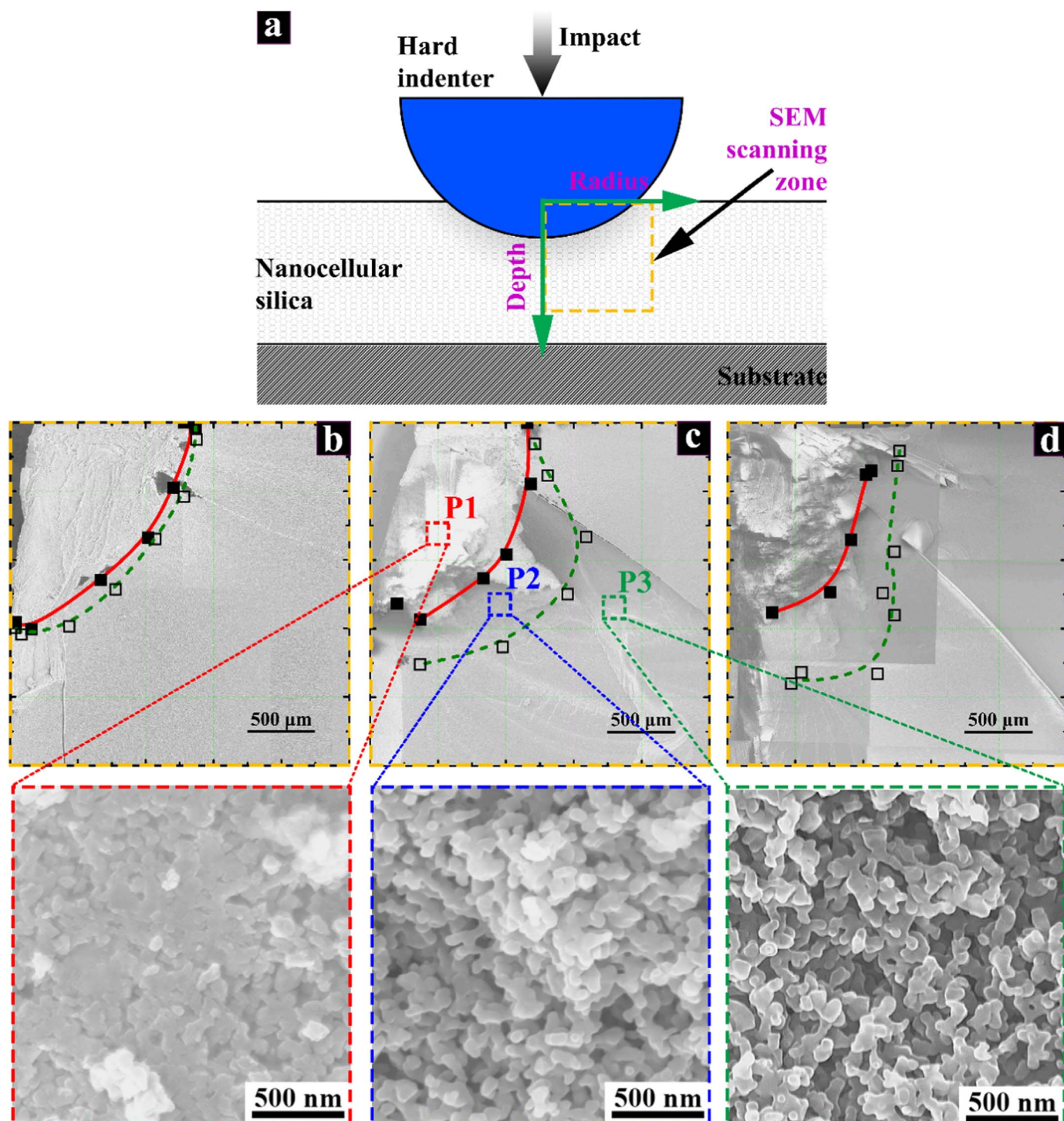


Fig. 8. SEM images of dynamically indented cellular silica samples. (a) Schematic of the SEM scanning zone. SEM scanning zones of cellular silica with the average cell sizes of (b) 275 nm, (c) 105 nm, and (d) 50 nm, respectively. The solid squares and the solid lines mark out the boundaries of cell deformation zones (CDZ); the hollow squares and the dashed lines mark out the boundaries of transition zone (TZ). The insets to (c), from left to right, show the cellular structures in the CDZ (P1), in the TZ (P2), and in the far field (P3), respectively. (For interpretation of the references to color in this figure legend, the reader is referred to the web version of this article.)

Dr. David M. Stepp. Special thanks are also due to Professors Marc A. Meyers and Vitali F. Nesterenko for the useful discussions.

Appendix A. Supporting information

Supplementary data associated with this article can be found in the online version at doi:10.1016/j.msea.2017.03.091.

References

- [1] L.J. Gibson, M.F. Ashby, *Cellular Solids: Structure and Properties*, Cambridge University Press, Cambridge, UK, 1997.
- [2] M. Scheffler, P. Colombo, *Cellular Ceramics: Structure, Manufacturing, Properties and Applications*, John Wiley & Sons, New York, 2006.
- [3] T. Mukai, H. Kanahashi, T. Miyoshi, M. Mabuchi, T.G. Nieh, K. Higashi, *Scr. Mater.* 40 (1999) 921–927.
- [4] J.S. Seo, D. Whang, H. Lee, S.I. Jun, J. Oh, Y.J. Jeon, K. Kim, *Nature* 404 (2000) 982–986.
- [5] Ö. Keleş, R.E. García, K.J. Bowman, *Acta Mater.* 61 (2013) 2853–2862.

- [6] W.-G. Bae, H.N. Kim, D. Kim, S.-H. Park, H.E. Jeong, K.-Y. Suh, *Adv. Mater.* 26 (2014) 675–700.
- [7] C. Zhao, Y. Qiao, *Mater. Sci. Eng.: A* 676 (2016) 450–462.
- [8] I. Vlahinić, J.J. Thomas, H.M. Jennings, J.E. Andrade, *J. Mech. Phys. Solids* 60 (2012) 1350–1362.
- [9] M. Borrega, L.J. Gibson, *Mech. Mater.* 84 (2015) 75–90.
- [10] L.J. Gibson, *J. Biomech.* 38 (2005) 377–399.
- [11] P. Fratzl, R. Weinkamer, *Prog. Mater. Sci.* 52 (2007) 1263–1334.
- [12] R.H. Baughman, A.A. Zakhidov, W.A. de Heer, *Science* 297 (2002) 787–792.
- [13] A.C. Pierre, G.M. Pajonk, *Chem. Rev.* 102 (2002) 4243–4266.
- [14] C.B. Park, A.H. Behraves, R.D. Venter, *Polym. Eng. Sci.* 38 (1998) 1812–1823.
- [15] D. Yuan, W. Lu, D. Zhao, H.-C. Zhou, *Adv. Mater.* 23 (2011) 3723–3725.
- [16] K. Nakanishi, *Synthesis Concepts and Preparation of Silica Monoliths, Monolithic Silicas in Separation Science: Concepts, Syntheses, Characterization, Modeling and Applications*, John Wiley & Sons, New York, 2010, p. 11.
- [17] B.C. Tappan, S.A. Steiner, E.P. Luther, *Angew. Chem. Int. Ed.* 49 (2010) 4544–4565.
- [18] L.R. Meza, A.J. Zelhofer, N. Clarke, A.J. Mateos, D.M. Kochmann, J.R. Greer, *Proc. Natl. Acad. Sci. USA* 112 (2015) 11502–11507.
- [19] S.J. Nam, J.Y. Hwang, H.-K. Kim, H.J. Choi, *Acta Mater.* 113 (2016) 170–179.
- [20] A.M. Hodge, J. Biener, J.R. Hayes, P.M. Bythrow, C.A. Volkert, A.V. Hamza, *Acta Mater.* 55 (2007) 1343–1349.
- [21] Z. Chen, X. Wang, F. Giuliani, A. Atkinson, *J. Am. Ceram. Soc.* 98 (2015) 2183–2190.
- [22] F. Svec, J.M. Fréchet, *Anal. Chem.* 64 (1992) 820–822.
- [23] A. Bhattacharya, V.V. Calmide, R.L. Mahajan, *Int. J. Heat Mass Transf.* 45 (2002) 1017–1031.
- [24] N. Leventis, C. Sotiriou-Leventis, G. Zhang, A.-M.M. Rawashdeh, *Nano Lett.* 2 (2002) 957–960.
- [25] L.J. Gibson, M.F. Ashby, *The Mechanics of Three-Dimensional Cellular Materials*, 1982.
- [26] J. Luo, R. Stevens, *Ceram. Int.* 25 (1999) 281–286.
- [27] M.M.J. Treacy, T.W. Ebbesen, J.M. Gibson, *Nature* 381 (1996) 678–680.
- [28] A.T. Jennings, M.J. Burek, J.R. Greer, *Phys. Rev. Lett.* 104 (2010) 135503.
- [29] B. Wu, A. Heidelberg, J.J. Boland, *Nat. Mater.* 4 (2005) 525–529.
- [30] Z.F. Ren, Z.P. Huang, J.W. Xu, J.H. Wang, P. Bush, M.P. Siegal, P.N. Provencio, *Science* 282 (1998) 1105–1107.
- [31] A.M. Hodge, J.R. Hayes, J.A. Caro, J. Biener, A.V. Hamza, *Adv. Eng. Mater.* 8 (2006) 853–857.
- [32] M. Hakamada, M. Mabuchi, *Scr. Mater.* 56 (2007) 1003–1006.
- [33] R.D. Shoup, *Controlled pore silica bodies gelled from silica sol-alkali silicate mixtures*, in: M. Kerker (Ed.) *Colloid and Interface Science*, Academic Press, New York, 1976, pp. 63–69.
- [34] K. Nakanishi, *J. Porous Mater.* 4 (1997) 67–112.
- [35] R. Miyamoto, Y. Ando, C. Kuru, H. Bai, K. Nakanishi, M. Ippommatsu, *J. Sep. Sci.* 36 (2013) 1890–1896.
- [36] C. Zhao, M. Wang, Y. Shi, J. Cao, Y. Qiao, *Mater. Des.* 90 (2016) 815–819.
- [37] Y. Diao, T. Harada, A.S. Myerson, T. Alan Hatton, B.L. Trout, *Nat. Mater.* 10 (2011) 867–871.
- [38] T. Kawaguchi, J. Iura, N. Taneda, H. Hishikura, Y. Kokubu, *J. Non-Cryst. Solids* 82 (1986) 50–56.
- [39] H. Kolsky, *Stress waves in solids*, Courier Corporation, 1963.
- [40] S. Nemat-Nasser, J.B. Isaacs, J.E. Starrett, *Proc. R. Soc. Lond. Ser. A: Math. Phys. Sci.* 435 (1991) 371–391.
- [41] B. Song, W. Chen, *Exp. Mech.* 44 (2004) 622–627.
- [42] C. Zhao, Y. Qiao, *Nanoscale* 8 (2016) 17658–17664.
- [43] W.C. Oliver, G.M. Pharr, *J. Mater. Res.* 19 (2004) 3–20.
- [44] P. Clément, S. Meille, J. Chevalier, C. Ollagnon, *Acta Mater.* 61 (2013) 6649–6660.
- [45] P.W. Bridgman, *Dimensional Analysis*, Yale University Press, New Haven, Connecticut, 1922.
- [46] P.J.S. Gash, *Tectonophysics* 12 (1971) 349–391.
- [47] R.C. Bradt, R.E. Tressler, *Fractography of Glass*, Springer, Berlin, Germany, 1994.
- [48] N. Kostyukov, *J. Appl. Mech. Tech. Phys.* 32 (1991) 967–973.
- [49] V. Nesterenko, Y.L. Luk'yanov, M. Bondar', *Combust. Explos. Shock Waves* 30 (1994) 693–695.
- [50] M.A. Meyers, *Dynamic Behavior of Materials*, John Wiley & Sons, New York, 1994.
- [51] V.F. Nesterenko, *Dynamics of Heterogeneous Materials*, Springer Science & Business Media, Heidelberg, Germany, 2001.
- [52] A. Leonard, C. Daraio, *Phys. Rev. Lett.* 108 (2012) 214301.

SUPPLEMENTARY MATERIAL

for

Enhanced Resistance of Nanocellular Silica to Dynamic Indentation

Cang Zhao ^{a,b}, Yu Qiao ^{a,c,*}

^a *Department of Structural Engineering, University of California - San Diego, La Jolla, CA 92093-0085, U.S.A.*

^b *X-ray Science Division, Argonne National Laboratory, Argonne, IL 60439, USA*

^c *Program of Materials Science and Engineering, University of California - San Diego, La Jolla, CA 92093, U.S.A.*

* *Corresponding author. Phone: 858-534-3388; Email: yqiao@ucsd.edu*

1. Mechanical Testing and Materials Characterization

1.1. Impact Testing System

Dynamic indentation tests of cellular and solid silica samples were conducted on an impact system [1, 2]. A Grade 9 Titanium (Ti) tube with the inner diameter, the outer diameter, and the length of 11.4 mm, 12.7 mm, and 462 mm, respectively, was used as the striker. Two 17-4 PH H900 stainless steel end-caps with the thickness of 5 mm were pressed into the two ends of the Ti tube, and were fixed by two stainless steel pins. The pins had a diameter of 3.2 mm and a length of 12.7 mm. The striker, together with the pins, had a total mass of 63 g. An AeroMarine polyurethane foam sleeve was employed to hold the striker inside the gas chamber. In this investigation, the pressure in the gas chamber was maintained at 15 psi, which results in a striker speed of $\sim 8.5 \text{ m s}^{-1}$. The striker speed was measured by two pairs of photomicro sensors (OMRON EE-SPW421).

Both the incident and the transmitted bars were made of 17-4 PH H900 stainless steel. The elastic modulus was 196.5 GPa, and the mass density was 7750 kg m^{-3} . The two bar diameters were the same 12.7 mm; their lengths were 178 cm and 152 cm, respectively. At the center of the two bars, two sets of strain gauges (Vishay WK-13-250BF-10C) were mounted to collect the stress wave signals through a data acquisition (DAQ) system (Vishay 2310B).

To ensure that the sample was only subjected to the first pulse loading, a momentum trapper system was developed [3, 4]. It included a rigid block, a flange attached to the impact end of the incident bar, and a two-piece thread-clamping locknut. Initially there was a gap between the rigid block and the flange. The gap width was accurately and precisely adjusted so that the motions of the flange, together with the incident bar, would be stopped immediately once the stress wave produced by the Ti tube striker had completely entered into the incident bar. Therefore, only a single pulse loading was applied to the silica sample.

1.2 Dynamic compression tests

In all the tests, the striker speed was maintained at $\sim 8.5 \text{ m/s}$. On the far end of the incident bar, a silica sample was attached, without the indenter, and the sample was supported from the back by the transmission bar. The one-dimensional stress wave subsequently entered the sample,

and the transmission bar. Typical incident, reflected, and transmitted waves are presented in Fig. S3 (a-c). The transmitted wave pressure is nearly constant, independent of the cell size (Fig. S3d).

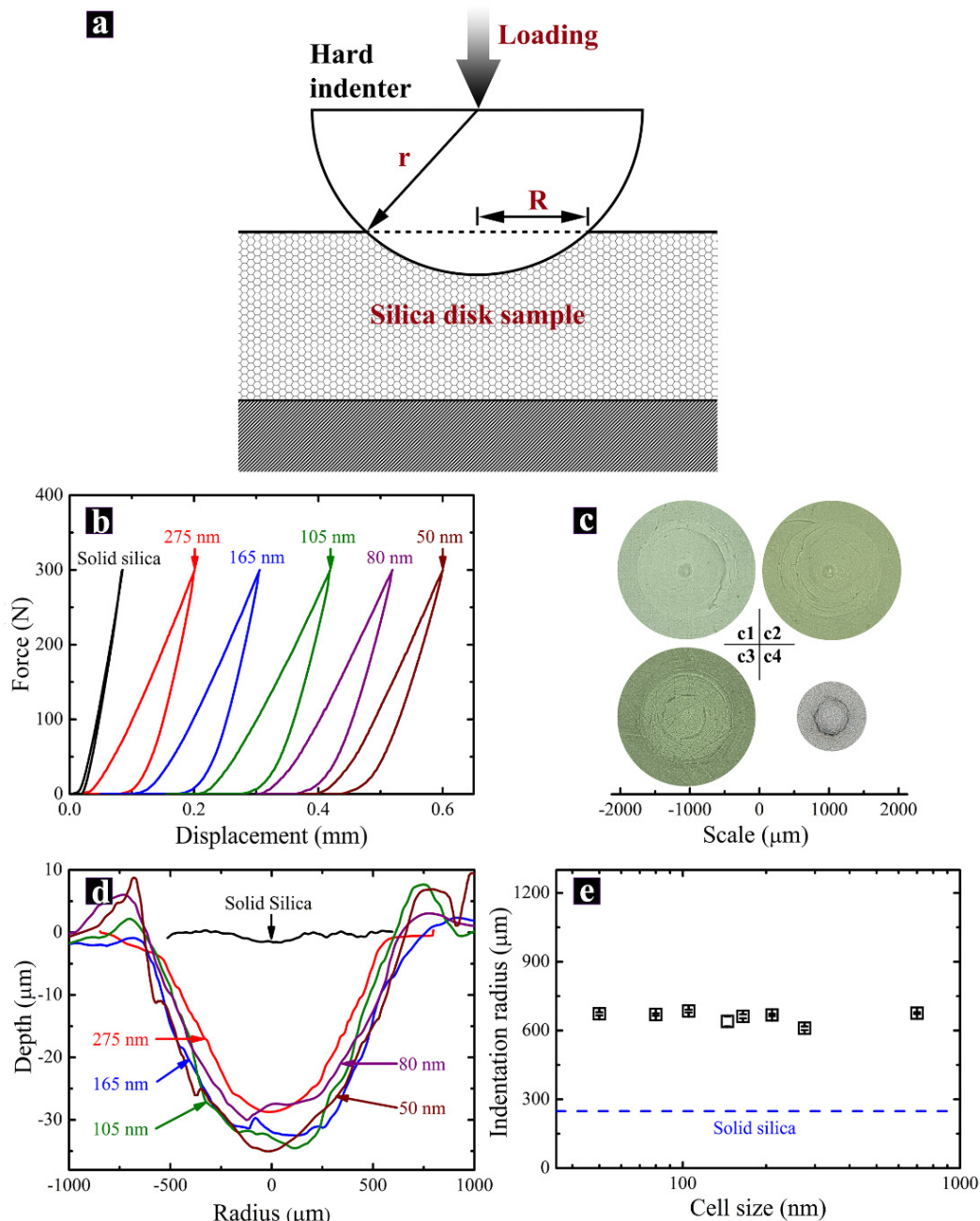


Fig. S1. Quasi-static indentation. (a) Schematic of the quasi-static indentation setup. (b) Typical indentation curves. The curves have been shifted along the horizontal axis. The arrows indicate the average cell sizes. (c) Photos of quasi-statically indented cellular silica samples with the average cell sizes of (c1) 275 nm, (c2) 105 nm, and (c3) 50 nm, respectively; (c4) is a solid silica sample. (d) Typical indentation depth profiles of quasi-statically tested samples; the arrows indicate the average cell sizes. (e) Indentation radius as a function of the average cell size. The blue dash line shows the average indentation radius of solid silica samples, with the standard derivation less than 2 μm .

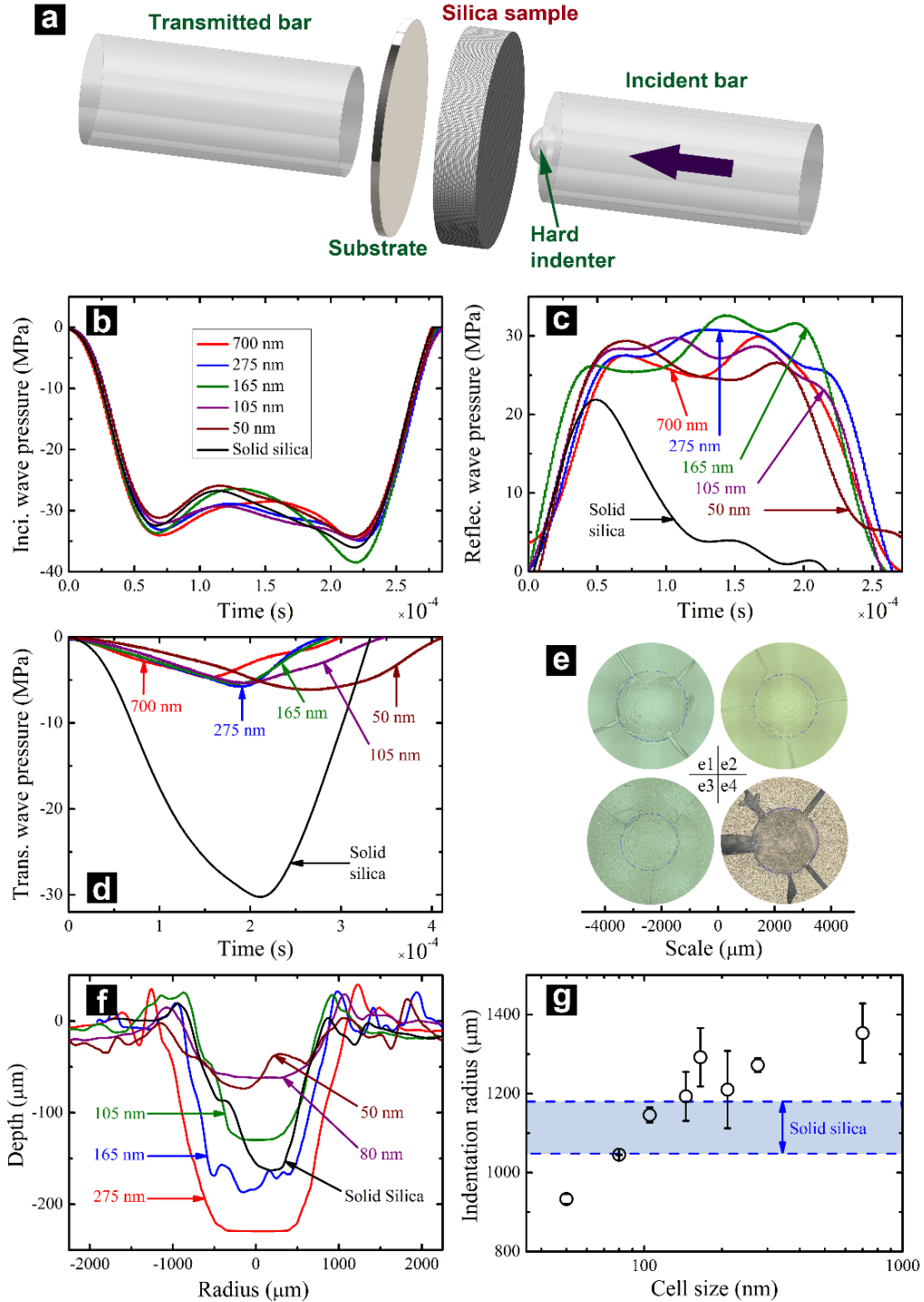


Fig. S2. Dynamic indentation. (a) Schematic of the dynamic indentation setup. The arrow indicates the impact direction of the striker. Typical profiles of (b) incident, (c) reflected, and (d) transmitted stress waves. (e) Photos of dynamically indented cellular silica samples with the average cell sizes of (e1) 275 nm, (e2) 105 nm, and (e3) 50 nm, respectively; (e4) is a solid silica sample. (f) Typical indentation depth profiles of dynamically tested samples. The arrows indicate the average cell sizes. (g) Indentation radius as a function of the average cell size. The horizontal band within the two dashed lines shows the range of indentation radius of solid silica.

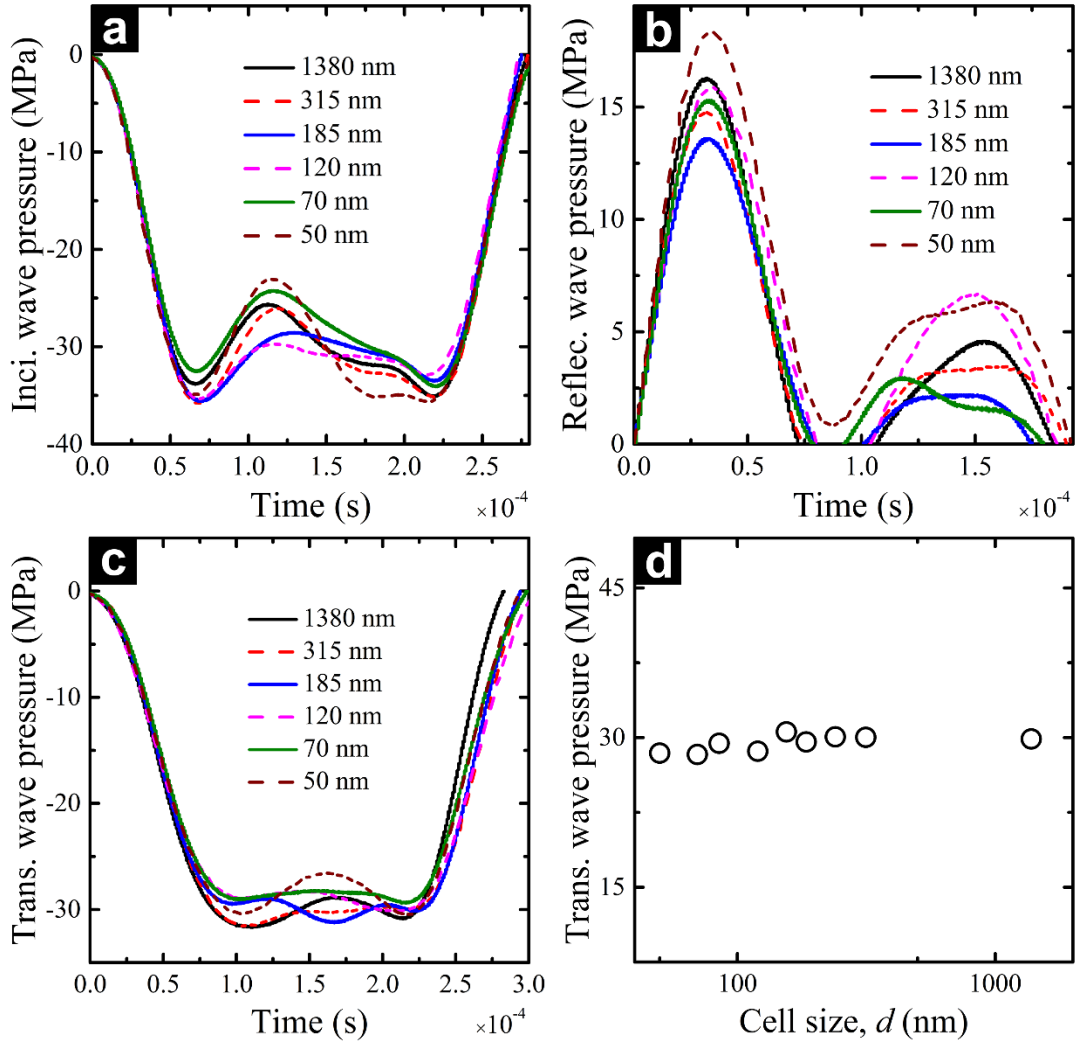


Fig. S3. Dynamic compression. Stress wave profiles of (a) incident waves (b) reflective waves and (c) transmitted waves. The numbers indicate the average cell sizes. (d) Peak pressure of transmitted waves as a function of the average cell size.

Table S1. Cellular structures in the cell deformation zones of dynamically indented nanocellular samples.

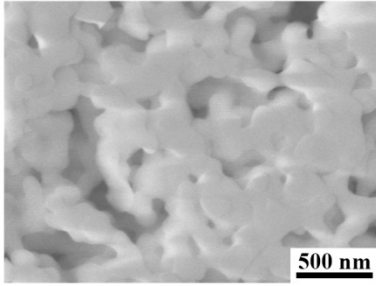
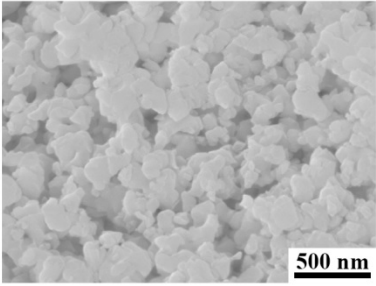
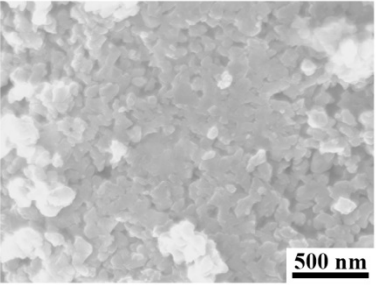
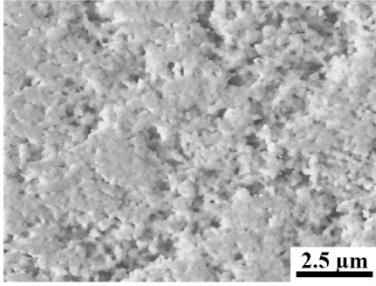
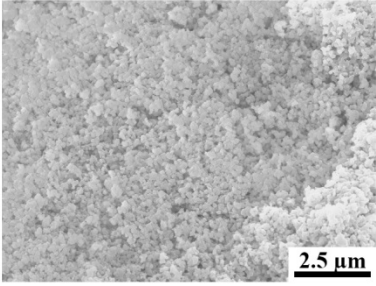
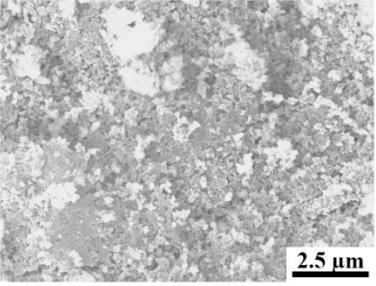
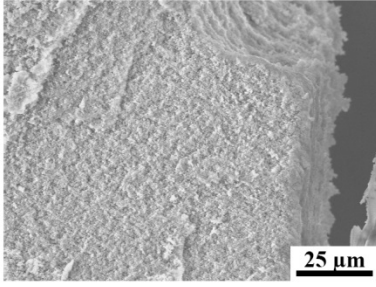
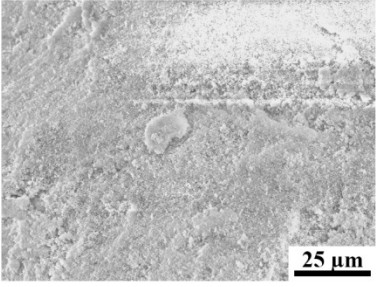
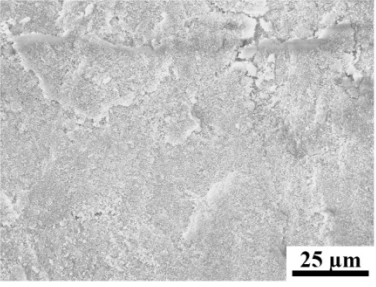
Magnification	Cell Size		
	275 nm	165 nm	105 nm
50000 X			
10000 X			
1000 X			

Table S2. Cellular structures in the transition zones of dynamically indented nanocellular samples.

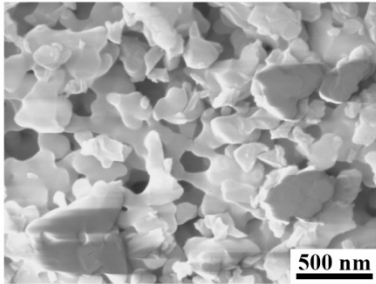
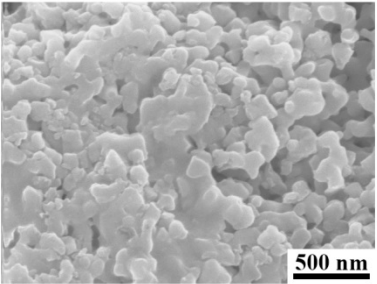
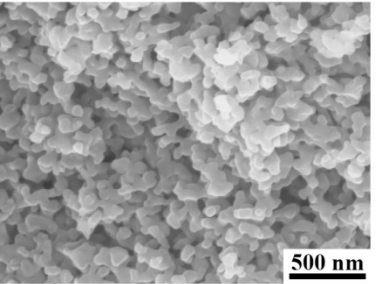
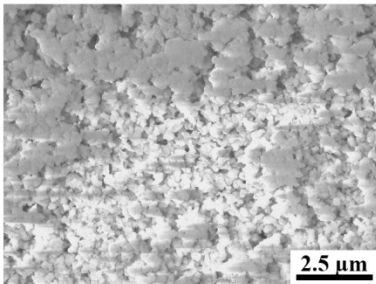
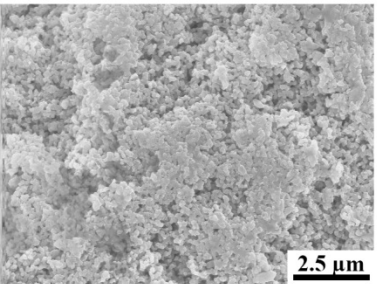
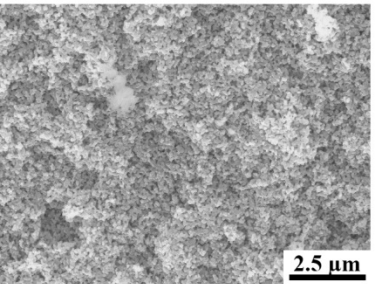
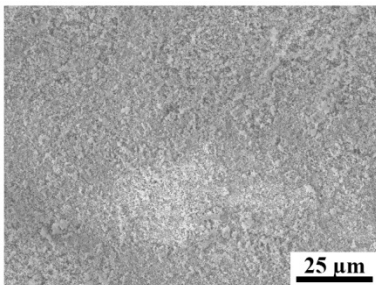
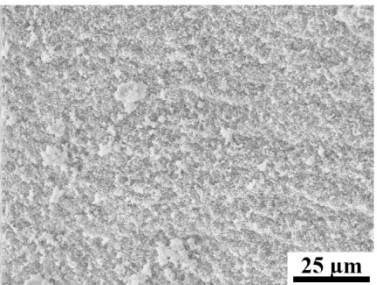
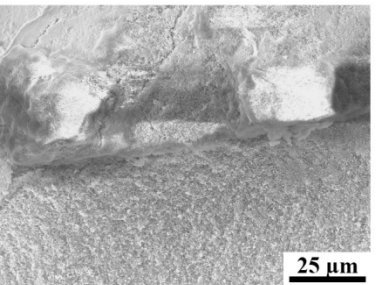
Magnification	Cell Size		
	275 nm	165 nm	105 nm
50000 X			
10000 X			
1000 X			

Table S3. Cellular structures in the far fields of dynamically indented nanocellular samples.

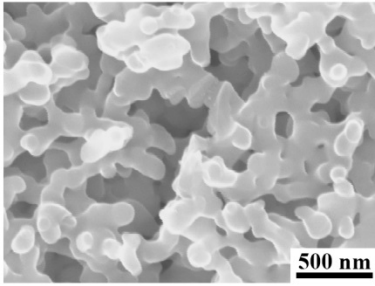
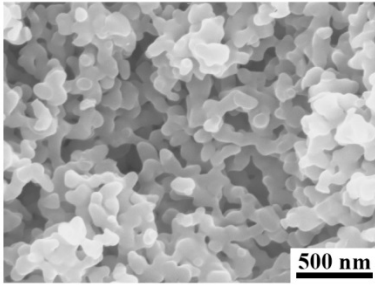
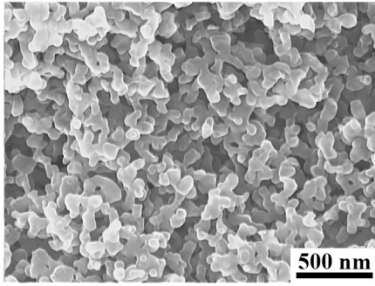
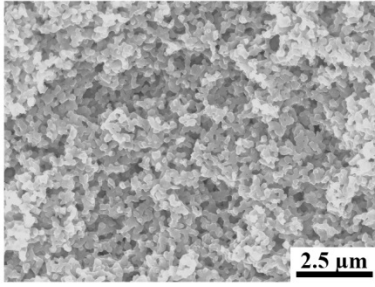
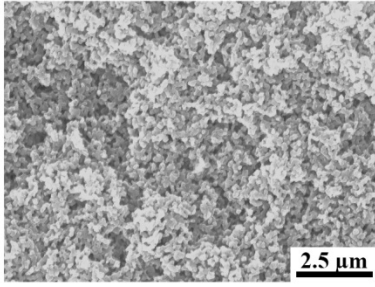
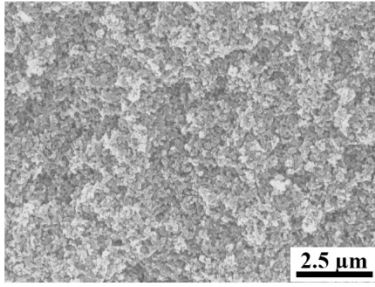
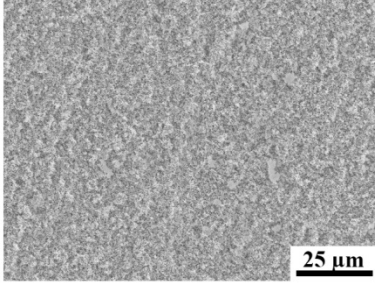
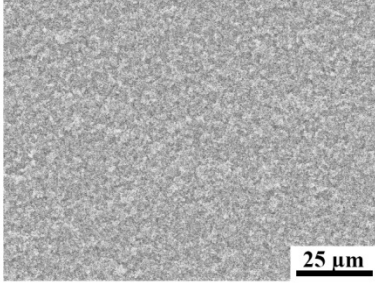
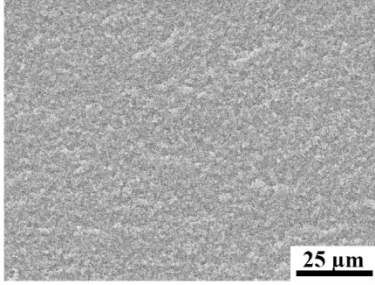
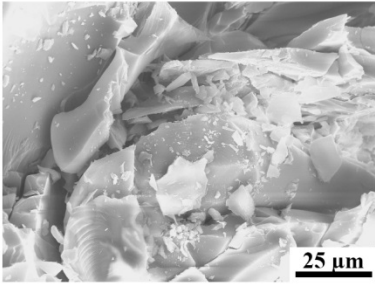
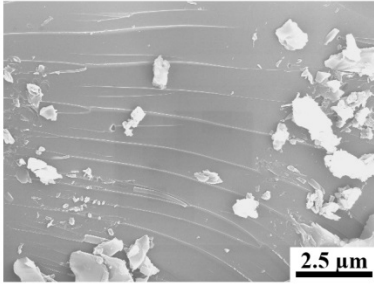
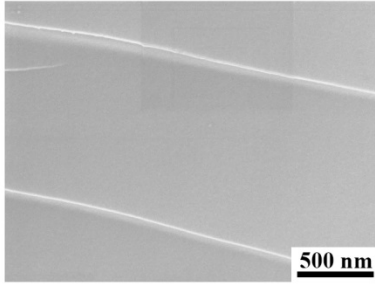
Magnification	Cell Size		
	275 nm	165 nm	105 nm
50000 X			
10000 X			
1000 X			

Table S4. Morphology of dynamically indented solid silica.

SEM Magnification		
1000 X	10000 X	50000 X
		

References

- [1] H. Kolsky. Stress waves in solids, Courier Corporation, 1963.
- [2] C. Zhao, Y. Qiao. Fast-condensing nanofoams: Suppressing localization of intense stress waves, *Materials Science and Engineering: A* 676 (2016) 450-462.
- [3] S. Nemat-Nasser, J.B. Isaacs, J.E. Starrett. Hopkinson techniques for dynamic recovery experiments, *Proceedings of the Royal Society of London. Series A: Mathematical and Physical Sciences* 435 (1991) 371-391.
- [4] B. Song, W. Chen. Loading and unloading split Hopkinson pressure bar pulse-shaping techniques for dynamic hysteretic loops, *Experimental Mechanics* 44 (2004) 622-627.